

Citation for published version:

Ahiavi, E, Dawson, JA, Kudu, U, Courty, M, Islam, MS, Clemens, O, Masquelier, C & Famprikis, T 2020, 'Mechanochemical synthesis and ion transport properties of Na₂OX (X = Cl, Br, I and BH₄) antiperovskite solid electrolytes', *Journal of Power Sources*, vol. 471, 228489. <https://doi.org/10.1016/j.jpowsour.2020.228489>

DOI:

[10.1016/j.jpowsour.2020.228489](https://doi.org/10.1016/j.jpowsour.2020.228489)

Publication date:

2020

Document Version

Peer reviewed version

[Link to publication](#)

Publisher Rights

CC BY-NC-ND

University of Bath

Alternative formats

If you require this document in an alternative format, please contact:
openaccess@bath.ac.uk

General rights

Copyright and moral rights for the publications made accessible in the public portal are retained by the authors and/or other copyright owners and it is a condition of accessing publications that users recognise and abide by the legal requirements associated with these rights.

Take down policy

If you believe that this document breaches copyright please contact us providing details, and we will remove access to the work immediately and investigate your claim.

Mechanochemical Synthesis and Ion Transport Properties of Na_3OX ($\text{X} = \text{Cl}, \text{Br}, \text{I}$ and/or BH_4) Antiperovskite Solid Electrolytes

Ernest Ahiavi^{1,2,3}, James A. Dawson^{4,5}, Ulas Kudu¹, Matthieu Courty¹, M. Saiful Islam^{5,6}, Oliver Clemens², Christian Masquelier^{1,3,6}, Theodosios Famprikis^{1,3,5,6}

¹ Laboratoire de Réactivité et de Chimie des Solides (CNRS UMR 7314), Université de Picardie Jules Verne, Amiens, France

² Technical University of Darmstadt, Materialdesign durch Synthese group, Department of Materials- and Earth Sciences, Alarich-Weiss-Str. 2, 64287 Darmstadt, Germany.

³ Réseau sur le Stockage Electrochimique de l'Énergie (RS2E CNRS FR 3459), Amiens, France

⁴ Chemistry – School of Natural and Environmental Sciences, Newcastle University, Newcastle upon Tyne, NE1 7RU, UK

⁵ Department of Chemistry, University of Bath, Bath BA2 7AY, United Kingdom

⁶ ALISTORE–European Research Institute (CNRS FR 3104), Amiens, France

Abstract: The push towards the development of next-generation solid-state batteries has motivated the search for novel solid electrolyte materials. Sodium antiperovskites represent a structural family of ion conductors that has emerged as a result, with expected advantages in terms of composition tuning, electrochemical stability, mechanical softness and high ionic conductivity. Here, we report the mechanochemical synthesis of several materials in this structural family, including novel mixed-halide compositions such as $\text{Na}_3\text{OCl}_{0.5}(\text{BH}_4)_{0.5}$, $\text{Na}_3\text{OBr}_{0.5}(\text{BH}_4)_{0.5}$, $\text{Na}_3\text{OI}_{0.5}(\text{BH}_4)_{0.5}$ and $\text{Na}_3\text{OCl}_{0.33}\text{Br}_{0.33}(\text{BH}_4)_{0.33}$. We rationalize the effect of halide substitution on the structure and ion transport properties of these materials. We conclude with a discussion on Na_3OBH_4 , which has recently been reported to be a fast ion conductor, owing to the rotational disorder of the complex superhalide anion BH_4^- . We are unable to reproduce the reported high ionic conductivity of Na_3OBH_4 neither by experiment nor ab initio simulation.

Keywords: synthesis; ball-milling; antiperovskite; borohydride; ionic conductivity; molecular dynamics

1. Introduction

Research into solid Li^+ - and Na^+ -ion conductors has rapidly escalated over the last decade in view of possible applications in solid-state batteries [1–3]. These efforts have afforded an increasing fundamental understanding of ion migration in the solid state along with the discovery of several previously disregarded families of materials that can sustain fast ion diffusion [4,5]. One such family of materials is characterized by the antiperovskite structural arrangement, typically denoted lithium- or sodium-rich antiperovskites, to differentiate from the much studied oxide perovskite lithium-ion conductors of the $\text{Li}_{3x}\text{La}_{\frac{1}{2}-x}\text{TiO}_3$ archetype [6,7].

With the latest Nobel prize awarded to pioneers of the lithium battery technology, it seems fitting to contribute to this celebratory issue with our work related to one of the laureates, John B. Goodenough, who has recently been involved in the development of solid-state batteries using antiperovskite electrolytes [8–10]. Furthermore, significant attention has been generated by high-profile publications on the antiperovskites Li_3OCl [11] and Na_3OBH_4 [12] claiming superb ionic conductivities of the order of mS/cm at room temperature for Li^+ and Na^+ , respectively.

The interest in the antiperovskite family as solid electrolytes for battery applications arises from several factors, including: i) a simple structural archetype that is prone to iso- and aliovalent substitutions and, as such, to property tailoring [13]; ii) the absence of (semi)metallic elements, which are at the root of reductive instability with battery anodes [1,14] (in this case Na metal). This leads to expectations of minimal electronic conductivity and electrochemical stability in battery conditions; iii) their soft mechanical properties [15], which are key to facile densification and integration in solid-state batteries. Furthermore, this allows the synthesis of these materials through mechanochemistry, as demonstrated in the present study; and iv) the aforementioned reports of high ionic conductivity [11,12] allowing highly efficient and fast charge-discharge cycles of a battery cell.

Stoichiometric Na antiperovskites Na_3CX typically include a chalcogenide (C) and a (super)halide (X), with the former and latter occupying the 6- and 12-fold coordinated anion sites, respectively. To our knowledge, the first sodium-rich antiperovskite reported was Na_3NO_3 (i.e. $[\text{Na}^+]_3[\text{O}^{2-}][\text{NO}_2^-]$) in 1983 by Zintl and Morawietz [16–18]. The archetypical Na_3OCl and Na_3OBr were then synthesized by Sabrowsky et al. 50 years later [19]. Jansen et al. studied the Na^+ conductivity of Na_3OBr , Na_3NO_3 and Na_3OCN and observed a sharp enhancement of ion transport above a transition temperature specific to each compound, as a signature of an order-disorder phase transition with respect to the orientation of the complex superhalogen anions NO_2^- and CN^- (paddle-wheel effect) [18,20,21]. Wang et al. first showed the possibilities for isovalent mixing in the halide site with $\text{Na}_3\text{OCl}_{1-x}\text{Br}_x$ ($0 < x < 1$) and $\text{Na}_3\text{OBr}_{1-x}\text{I}_x$ ($0 < x < 0.6$), as well as aliovalent substitution of Na^+ with Ca^{2+} , Sr^{2+} to increase Na^+ conductivity [22]. Nguyen et al. highlighted a considerable secondary contribution to the ionic impedance of Na_3OBr , attributable to imperfect particle contact, which they alleviated through spark plasma sintering [23].

Understanding of the atomistic ion conduction mechanisms at play in antiperovskites has mostly been pursued by computational means [24,25]. Whether alkali vacancies or interstitials are the dominant charge carriers in the antiperovskite structure has been a matter of debate [26]. Studies on the defect energetics on Na_3OCl point to NaCl Schottky (pairs of Na^+ and Cl^- vacancies) as the dominant defects [27,28], whereas, Zhu et al. proposed Na_2O Schottky defects (pairs of 2Na^+ and O^{2-} vacancies) for Na_3OBr on the basis of neutron diffraction [29]. In any case, sodium vacancies seem to be the majority Na^+ defect species in sodium-rich antiperovskites. Theoretical works have also examined the effect of lattice distortions (including symmetry breaking from the cubic aristotype structure) on the phase

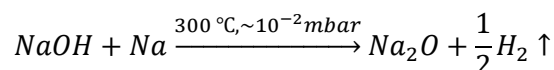
stability and ion transport [30,31]; still, such distorted alkali anti-perovskites remain elusive experimentally.

Considerable computational efforts have also been directed towards the prediction of compositions and design strategies to guide further experimental efforts. A well accepted strategy that has also been confirmed experimentally is the aliovalent substitution of divalent M^{2+} on the Na^+ sites so as to create Na vacancies ($M = Mg^{2+}$, Ca^{2+} , Sr^{2+} and so on) [22,27]. Beyond doping, notable compositions to target experimentally are $Na_3O_{0.5}S_{0.5}I$ [32] Na_3SI [31] and Na_3SBCl_4 [33], which utilize larger chalcogen and halide ions to increase the lattice volume and enlarge the diffusion pathways for sodium. Another composition of particular interest is also the inverted antiperovskite Na_3FS in which the large chalcogen would occupy the 12-fold coordinated anion site and small halogen the 6-fold coordinated anion site [31]. Beyond studies in the framework of ion conductors, other sodium-rich antiperovskites have also been reported, including $Na_3(SO_4)F$ [34] and $Na_2(BH_4)(NH_2)$ [35], for which no ionic conductivity data have been collected.

In the present study, we report on our efforts aimed at i) demonstrating the efficiency of mechanochemistry as a novel synthetic route for these soft sodium antiperovskite materials; ii) synthesizing for the first time binary- and ternary halide mixtures including BH_4^- ; iii) providing a holistic discussion of the structure-property relationships in Na-rich antiperovskites, integrating our results in the context of previous findings; and iv) attempting to reproduce and build on the recent promising reports on Na_3OBH_4 .

2. Methods

Synthesis of sodium oxide (Na₂O). Although anhydrous (super)halides (NaX) are readily available, commercial Na₂O reagents often contain significant amounts of impurities, mainly sodium peroxide (Na₂O₂) and hydroxide (NaOH) (Figure 1a). In previous reports, such commercial powders have been used in the synthesis of Na₃OX antiperovskites, in conjunction with excess Na metal [22,23] and/or under vacuum [23] to alleviate this issue, assuming the evacuation of H₂, O₂ or H₂O. Here, we have opted to produce ‘homemade’ Na₂O reagent as a first step, by reduction of NaOH by metallic Na (excess), similar to a recent study [29], according to:



The reagents were thoroughly mixed using an agate mortar and pestle in an Ar-filled glovebox. The mixture was then loaded into an alumina boat and heated in a vacuum oven (Büchi) connected to a vacuum pump at 300 °C for 14 h. The produced hydrogen gas was evacuated and excess sodium metal deposited on a cold trap. This procedure was repeated four times to drive the reaction to completion. This synthesis resulted in pure Na₂O, free of the aforementioned impurities, as attested by the associated x-ray diffractogram (Figure 1b).

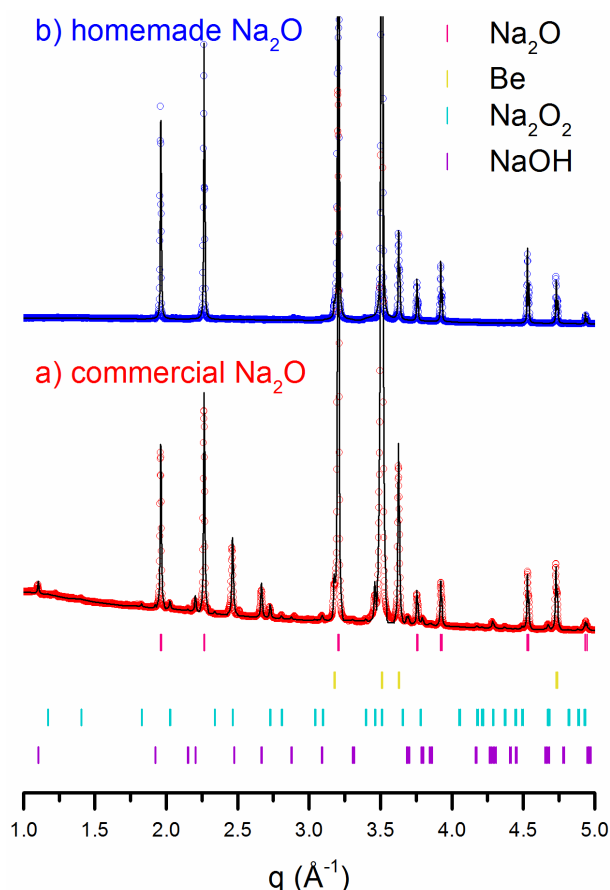
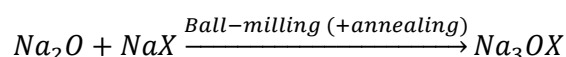


Figure 1: X-ray diffractograms of a) commercial and b) ‘homemade’ Na₂O, including profile fits. Samples were placed within a moisture- and air-free cell capped with a Be window. Measured Na₂O₂ and NaOH impurities present in the former are absent in the latter.

Synthesis of Na₃OX antiperovskites. The ‘homemade’ Na₂O and commercial NaCl (Acros Organics 99.5%), NaBr (Acros Organics 99+%), NaI, NaBH₄ powders were utilized as reagents. Prior to the synthesis, all reagents used were dried under vacuum at 100 °C for 24 h in a glass vacuum oven (Büchi) to remove residual moisture. Equimolar mixtures of pure Na₂O and NaX (X = Br, Cl, I, BH₄) were thoroughly ground into fine powders in an Ar-filled glovebox. The precursor powders (typically 1.5 g) were loaded into an 80 mL ZrO₂ milling jar containing twelve 10-mm-diameter ZrO₂ balls (total mass 36 g). A planetary ball mill (Fritsch Pulverisette 7 Premium) was used for the mechanochemical synthesis at 600 rpm for a total effective milling time of 24 h with a 5 min pause every 20 min of milling. Samples produced in this way are referred to as ‘as-milled’.



To improve crystallinity, the ball-milled antiperovskite powders were hydraulically pelletized (370 MPa) into 13-mm-diameter pellets using a stainless-steel die and annealed in a glass vacuum oven (Büchi) for 13 h at 200 °C under vacuum. Samples produced this way are referred to as ‘annealed’.

X-ray powder diffraction. Diffractograms of all antiperovskite samples were measured at room temperature using a Bruker D8 diffractometer with Cu-K α or Co-K α radiation ($\lambda_{\text{Cu}} = 1.5418 \text{ \AA}$ and $\lambda_{\text{Co}} = 1.7903 \text{ \AA}$, respectively). The moisture-sensitive powders were placed in hermetic sample holders under Ar atmosphere in a glove-box. Depending on the sample holder, diffractograms were collected either through a $\approx 100 \text{ }\mu\text{m}$ Be window or through a dome-shaped PEEK cap. The former produces a flat background but attenuates the intensity of Bragg reflections non-uniformly (decreasing absorption with 2θ); the latter produces significant diffuse scattering at low 2θ but does not affect the relative intensity ratio of Bragg reflections along. Fitting of the diffractograms was performed with the Le Bail and Rietveld methods as integrated in the FullProf and Jana 2006 software suites.

Impedance spectroscopy. Measurements of electrochemical impedance spectroscopy were made using a frequency response analyser (MTZ-35, Biologic) and an intermediate temperature system (ITS, Biologic). Annealed samples were first pelletized using a 13 mm die in a uniaxial hydraulic press (typically $\sim 750 \text{ MPa}$). The pellets (80-90% dense) were then sandwiched between two graphite paper disks which served as blocking electrodes. The pellets were loaded in an Ar-filled glovebox into a hermetic sample holder (CESH, Biologic) and measured at temperatures ranging from 25 to 100 °C. A frequency range of 30 MHz to 0.1 Hz and an excitation voltage of 0.05 V were utilized. The ionic conductivities were determined by extracting the resistances from the Bode plots (as explained in ref. [36]) and calculating the conductivities taking the dimensions of the pellets into account. The activation energy (E_a) for Na ion diffusion was calculated from the slope of the Arrhenius plot.

Thermal analysis. Coupled differential scanning calorimetry (DSC) and thermogravimetric analysis (TGA) measurements were performed using a NETZSCH STA 449F3 Jupiter housed in an Ar-filled glovebox. Heating and cooling rates of 10 °C/min were utilized, under a constant flow of Ar (50 mL/min). The mass spectra of the evolved gases were recorded using a mass spectrometer.

Vibrational spectroscopy. Infrared spectra were recorded at ambient temperature using a Thermo Scientific (Nicolet iS10) FT-IR. The borohydride samples were mixed with dry KBr (ca. 90 wt.% KBr and 10 wt.% Na₃OBH₄/NaBH₄) and pelletized using a 13 mm stainless-steel die and sealed in an air-tight sample holder in an Ar-filled glovebox prior to data acquisition on the antiperovskite. All spectra were recorded in the region 4000–400 cm⁻¹ and the KBr spectrum was subtracted. Raman spectra were acquired using a Raman DXR Microscope (Thermo Fisher Scientific) with an excitation laser beam ($\lambda = 532 \text{ nm}$) at 1 mW laser power using a pinhole slit (25 μm). Na₃OBH₄ and NaBH₄ powders were

loaded on glass slides and covered with electrical tape in an Ar-filled glovebox. Spectra were collected through glass slides in the range 50–3500 cm⁻¹.

Ab initio molecular dynamics (AIMD) simulations. The simulations in this work were carried out using density functional theory (DFT) with the Vienna ab initio simulation package (VASP) [37]. A plane-wave cut-off energy of 400 eV was utilized. The projector augmented wave method [38] and the PBEsol exchange-correlation functional [39] were employed for all calculations. The k-space was sampled using the gamma-point only with 3×3×3 supercells containing 243 and 135 atoms for Na₃OBH₄ and Na₃OX (X = Cl, Br or I), respectively. To induce Na-ion transport, Na vacancies were added to each supercell at a concentration of 5%. Statistical properties were obtained from simulations of >50 and >100 ps for Na₃OBH₄ and Na₃OX (X = Cl, Br or I), respectively, using the NVT ensemble with the Nose–Hoover thermostat [40]. The AIMD calculations for Na₃OBH₄ were carried out at 600, 700 and 800 K, with a time step of 1 fs to account for the protons. Temperatures above 800 K were tested but resulted in structural instabilities with protons separating from the BH₄ tetrahedra. A similar issue was also found by Sun et al. at 1100 K [37]. For Na₃OX (X = Cl, Br or I), the simulations were run at 600, 800 and 1000 K, with a time step of 2 fs. Self-diffusion data for Na were obtained from the mean square displacement (MSD) according to:

$$\langle r_i^2(t) \rangle = 6D_{Na}t$$

where $\langle r_i^2(t) \rangle$ is the MSD, D_{Na} is the diffusion coefficient for Na and t is time. Activation energies for Na-ion diffusion were extracted by fitting to an Arrhenius relationship of the form:

$$D_{Na} = D_0 e^{-E_a/kT}$$

where D_0 is the Arrhenius prefactor.

3. Results and Discussion

3.1. Mechanochemical synthesis of Na₃CX antiperovskites

A commonly-cited stability criterion for the stability of perovskite structures is the tolerance factor, t , introduced by Goldschmidt [41], involving a simple geometrical consideration of the ionic radii of the constituent atoms. For an ABO₃ oxide perovskite (and by extension a XCNa₃ sodium-rich antiperovskite such as ClONa₃), it can be written as:

$$t = \frac{r_A + r_O}{\sqrt{2}(r_B + r_O)} = \frac{r_X + r_{Na}}{\sqrt{2}(r_C + r_{Na})}$$

where r_i is the ionic radius of atom i . $t = 1$ corresponds to the ideal case of the three ions fitting perfectly in a cube. Deviations from unity indicate size mismatch between the ions and can lead to phase instability and/or distortions from the cubic (anti)perovskite aristotype.

By analogy to classical oxide perovskites, it might be assumed that a range of $0.85 < t < 0.95$ might be ideal for such structures, and as such might serve as an adequate predictor of stability for further material development. Figure 2 summarizes the synthesizability of sodium-rich antiperovskites as a function of constituent anion size, including our attempts through mechanochemistry.

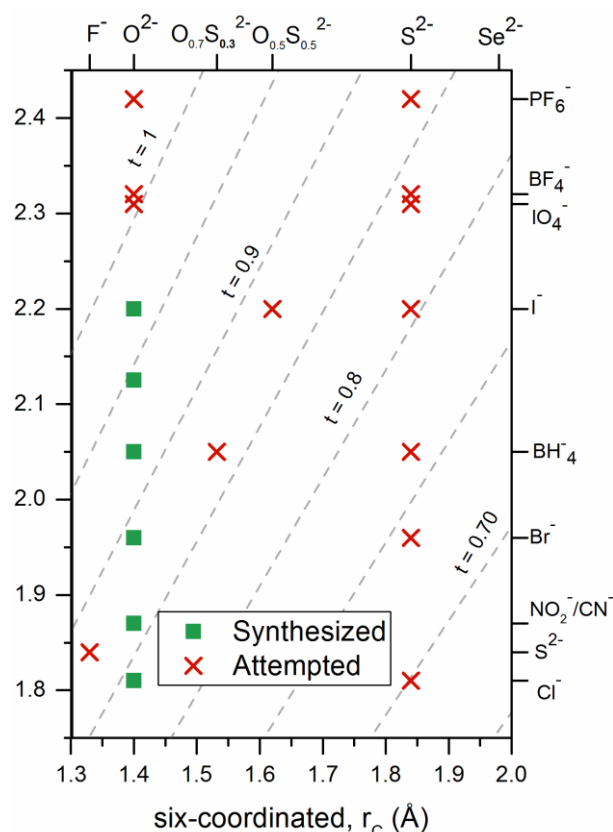


Figure 2: Summary of Na_3CX synthesizability as a function of 6-coordinated (F^- , O^{2-} , S^{2-} and Se^{2-}) and 12-coordinated (Cl^- , S^{2-} , NO_3^- , CN^- , Br^- , BH_4^- , I^- , IO_4^- , BF_4^- and PF_6^-) anion sizes. Dotted diagonals represent values of the tolerance factor t .

Multiple oxide antiperovskites Na_3OX are synthesizable within a wide range of tolerance factors $0.84 < t < 0.97$. The limit of stability for Na_3OX seems to be around $t = 1$, i.e., for superhalogens X that are excessively large like IO_4^- , BF_4^- and PF_6^- . Since the size of the two anions greatly influences the lattice volume, Na_3OI should then be the the oxide sodium-rich antiperovskite with the highest molar volume. Assuming that higher molar volume could be correlated with ion enhanced transport, it would be desirable to increase it further by replacing O^{2-} with larger anions on the 6-coordinated site. The natural choice is S^{2-} and previous computational studies have identified $\text{Na}_3(\text{O}_{0.5}\text{S}_{0.5})\text{I}$ [32] and Na_3SI [31] as promising (oxy)sulfide materials to be synthesized.

As shown in Figure 2, despite multiple attempts, S^{2-} -containing compositions could not be successfully synthesized with the methodology described in this study. Due to the size of S^{2-} , sulfide Na_3SX antiperovskites have much lower tolerance factors with normal halides X. For example, the tolerance factor of Na_3SI is 0.81. For this reason we also attempted to prepare sulfide compositions with larger superhalides. Still, all attempts on synthesizing pure-sulfide Na_3SX proved unsuccessful, in contrast to oxide compositions with similar tolerance factors. For example, Na_3SPF_6 has a similar tolerance factor to Na_3OCN . Further, our exploratory synthesis efforts also covered other sulfide compositions identified by computational studies, such as Li_3SI [31] and Na_3FS [31] and $\text{Na}_3(\text{O}_{0.5}\text{S}_{0.5})\text{I}$, whose synthesis, also proved unsuccessful using our mechanochemical approach. It is obvious from Figure 2 that the tendency for synthesizability seems to be more correlated to the type of element occupying the 6-coordinated site rather than to the tolerance factor (Na_3OX are synthesizable over a wide range of tolerance factors from ~ 0.8 to 1). It is unclear at this point why Li- or Na- sulfide antiperovskites remain so elusive and therefore the Goldschmidt tolerance factor based on ionic radii is not a sufficient

criterion for the stability of sodium-rich antiperovskites. This fact might also be due to an intrinsic limitation of predicting accurately the Na-C and Na-X bond lengths in such systems: as discussed below, a spherical ion approximation might not be applicable.

We note, nevertheless, that our attempt at an oxysulfide composition with a modest sulfide content $\text{Na}_3\text{O}_{0.7}\text{S}_{0.3}\text{BH}_4$ yielded a semi-positive result, producing a cubic material indexed in the space group $Pm\bar{3}m$ with $a = 4.68 \text{ \AA}$ (Figure S2). This is larger than the 4.64 \AA of the pure oxide Na_3OBH_4 indicating some incorporation of sulfur in the structure. Such doping of S in oxide sodium-rich antiperovskites should be studied further in the future.

We target our discussion on the Na_3OX oxyhalide antiperovskites, which can be perceived as equimolar eutectic solutions of the Na_2O and NaX binaries and synthesized from the latter. Here, ‘homemade’ Na_2O (Figure 1) was used for the synthesis of Na_3OX in a closed-system to ensure purity without the need to evacuate side-products. A distinct advantage of the mechanochemical route is that there is no need for a high temperature treatment; using ball-milling alone the reactions can be driven to completion while, for reference, previous studies report on utilizing temperatures in the range of 300-600 °C [12,18,19,22,23,29,42]. The success of the mechanochemical route is probably linked to the soft nature of these materials (e.g. bulk modulus of $\sim 35 \text{ GPa}$ for Na_3OCl and Na_3OBr [15]).

The high-energy ball-milling of equimolar mixtures of Na_2O and NaX results in the straightforward synthesis of Na_3OX antiperovskites. This is evident from the diffractograms gathered in Figure 3, which can all be indexed in the $Pm\bar{3}m$ space group. Equimolar mixtures of two or three halides can also be used to produce single-phase antiperovskites. We have prepared in this way for the first time binary- and ternary-mixed-halide antiperovskites Na_3OX including BH_4^- , namely with $X = \text{Cl}_{0.5}(\text{BH}_4)_{0.5}$, $\text{Br}_{0.5}(\text{BH}_4)_{0.5}$, $\text{I}_{0.5}(\text{BH}_4)_{0.5}$ and $\text{Cl}_{0.33}\text{Br}_{0.33}(\text{BH}_4)_{0.33}$.

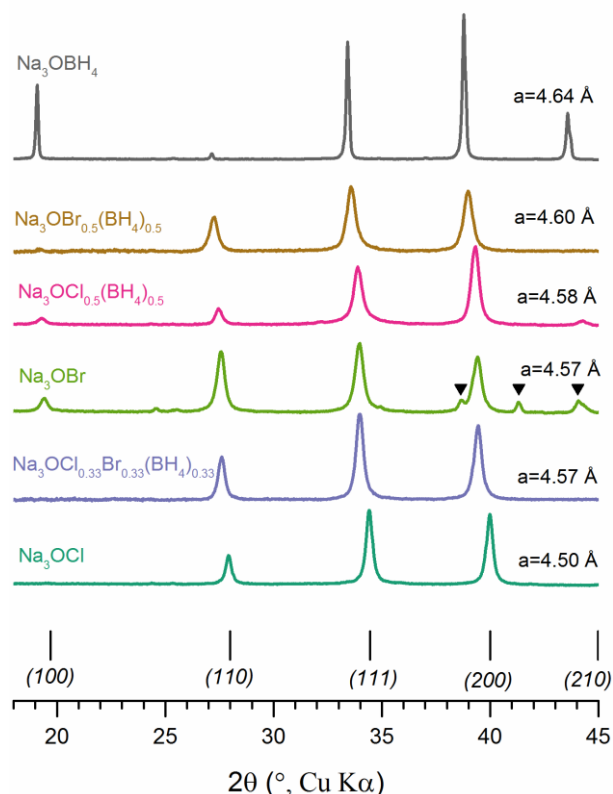


Figure 3. X-ray diffractograms of annealed antiperovskites in order of increasing lattice parameter. Bragg peak positions correspond to the $Pm\bar{3}m$ space group. $\text{Na}_3\text{OCl}_{0.33}\text{Br}_{0.33}(\text{BH}_4)_{0.33}$ and $\text{Na}_3\text{OBr}_{0.5}(\text{BH}_4)_{0.5}$ samples were measured in PEEK-dome cells and the associated diffuse scattering was subtracted as background. The

remaining samples were measured through an airtight sample holder featuring a Be window. BeO peaks in the Na₃OBr samples originate from slight oxidation of the Be and denoted with ▼.

As seen in Figure 3, the Bragg reflections indexed in the $Pm\bar{3}m$ space group shift to lower 2θ angles (higher d_{hkl}) as the halide anion X increases in size, indicating isotropic expansion of the unit cell. The relative peak intensities vary considerably with composition, owing to constructive/destructive interference linked to the ratio of the atomic scattering factors of oxygen and the (super)halogen(s). Both the relative intensity variation and the evolution of the lattice volume serves as proof of the integration of multiple halides in the structure of the binary and ternary compositions

3.2. Structure of Na₃OX

In an ideal cubic antiperovskite, oxygen is placed at (0, 0, 0) and sodium at (0, ½, 0), so that $d_{Na-O}=a/2$. Using the tabulated ionic radii [43] for Na⁺ and O²⁻, each in octahedral coordination (and assuming $t=1$), the expected sodium-oxygen distance is 2.34 Å and, consequently, the lattice parameter of each oxide antiperovskite Na₃OX should ideally be 4.68 Å. From **Figure 4**, it is evident that the lattice parameter and as such the effective sodium-oxygen distance, is actually in all cases lower than the nominal one (except for Na₃OI). Similarly, the sodium-(super)halide distance is always significantly larger than expected.

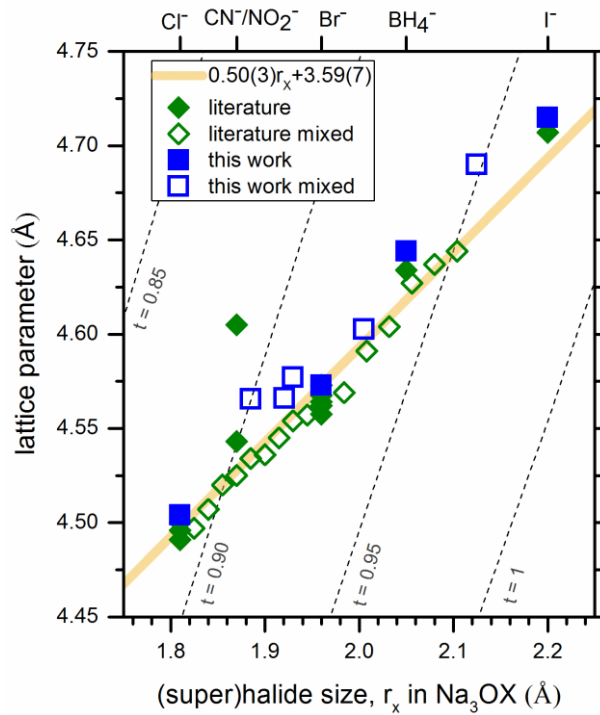


Figure 4: Relation between (super)halogen anion size, r_x , and cell parameter, a , of cubic Na₃OX sodium-rich antiperovskites. Data sorted depending on their provenance (literature or this work) and based on whether they correspond to a mixed-halide composition. Literature data included from Wang et al. (Na₃OCl_{1-x}Br and Na₃OBr_{1-x}I) [22], Hippler et al. [42] (Na₃OCl), Jansen et al. (Na₃ONO₂ [18] and Na₃OCN [20]), Sabrowsky et al. [19] (Na₃OCl and Na₃OBr), Zhu et al. [29] (Na₃OBr), Nguyen et al. [23] (Na₃OBr) and Sun et al. [12] (Na₃OBH₄). Dotted lines represent different values of the tolerance factor calculated using $r_{Na^{VI}}=1.02$ Å and $r_{O^{VI}}=1.40$ Å [43]. The yellow line represents a linear fit across all data points.

This observation should be interpreted in the framework of the unique Na coordination in Na₃OX antiperovskites, that is NaO_{2/6}X_{4/12} (each Na 6-coordinated by two oxygen and four halide ions). This seems to produce, in all cases, shorter Na-O and longer Na-X bonds than would be expected from

regular NaO_6 and NaX_6 octahedra, e.g. in Na_2O and NaX crystals. This ‘mismatch’ is implicitly captured in the tolerance factor (for all cases $t < 1$) and is alleviated as the X anion becomes larger (i.e. t tends to 1 moving from Cl to I). This mismatch might also suggest a non-negligible degree of covalent interaction between constituents, undermining the spherical-ion approximation central to the idea of ionic radii.

From Figure 4, it is obvious that the cubic lattice parameter is actually a function of the (super)halogen anion size. In other words, the smaller the halogen the more tightly the Na is bound to oxygen and vice-versa, and this should have distinct implications on ion transport. Nevertheless, a linear relationship is apparent between the ionic radius of the (super)halogen and the lattice parameter of the Na_3OX antiperovskite, resulting in a Vegard-type behavior. From the data points in Figure 4, we determine this linear relationship to be $a = 0.50 \cdot r_X + 3.59$. Out of the hitherto reported Na_3OX antiperovskites, $\text{Na}_3\text{O}(\text{NO}_2)$ seems to be the single outlier to this relationship. This is likely related to the difficulty in assigning unambiguous ionic radii to polyatomic anions in the framework of a spherical anion approximation. We emphasize that tabulated thermochemical radii [44] were used for the complex anions in this analysis.

3.3. Ion transport in Na_3OX

The impedance spectra of the annealed sodium-rich antiperovskites were measured as a function of temperature to derive activation energies using a typical Arrhenius relation. The resulting conductivities are plotted in **Figure 5a**. In addition, AIMD simulations were performed on several compositions and the Na^+ -diffusivities were extracted and plotted in **Figure 5b**.

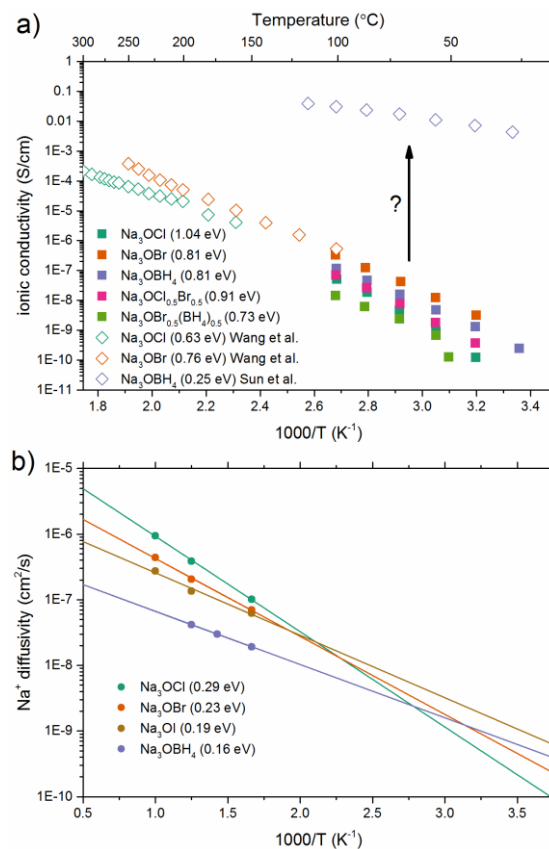


Figure 5: Arrhenius plots of (a) conductivity and (b) diffusivity for several Na_3OX antiperovskites. Conductivities in (a) measured by impedance spectroscopy. Na^+ diffusivities in (b) extracted from AIMD simulations. The activation energies E_a were derived by the slope of the linear fit of $\ln(\sigma T)$ or $\ln(D)$ versus $1/T$.

The conductivities measured in this work for Na₃OX samples all lie in the range 10⁻¹⁰ - 10⁻⁸ S/cm at room temperature and increase to about 10⁻⁸ - 10⁻⁶ S/cm at 100 °C. These values are in line with reports in literature except for Na₃OBH₄, which will be discussed separately below. Ball-milling sodium-rich antiperovskites does not seem to dramatically affect their ionic conductivity, as has been observed for other topical ion conductors, e.g. many members of the Li-P-S family [45].

It is clear that the calculated activation energies (0.16–0.29 eV) for Na-ion diffusion are significantly lower than the activation energies for conductivity (~0.6–1.0 eV) derived from impedance measurements. This is a common feature in the literature, with the vast majority of computational studies underestimating Na- and Li-ion activation energies in anti-perovskite solid electrolytes. This has been partially explained in a previous study by the presence of highly-resistive grain boundaries in experimental samples [24]. Such an interpretation is also consistent with the spread of reported conductivities and activation energies reported for the most studied compositions Na₃OCl and Na₃OBr. We conclude that the experimentally measured ion transport parameters of sodium rich antiperovskites are quite sensitive to details in the experimental procedures of pellet preparation and measurement of impedance spectra, as shown and discussed recently for a variety of ion conductors [46].

Although the measured conductivities are quite low in view of practical application, their comparison can yield fundamental understanding to guide further development of this family of materials. Figure 6 compares the ionic conductivity at 100 °C and the activation energy of sodium-rich antiperovskites against the size of the halide anion. A qualitative trend is observed: increasing halide size leads to increasing the conductivity and decreasing the activation energy. The conductivity trend can be rationalized based on the greater cell volume concomitant with increasing halide size (Fig. 6). The activation energy trend can be attributed to the polarizability of the larger ion which renders the lattice softer. Similar trends have been observed on multiple solid electrolyte systems, e.g. the (thio)LISICONs [47] and the Li₆PS₅X (X = Cl, Br or I) argyrodites [48]. These trends are qualitatively reproduced by our AIMD simulations.

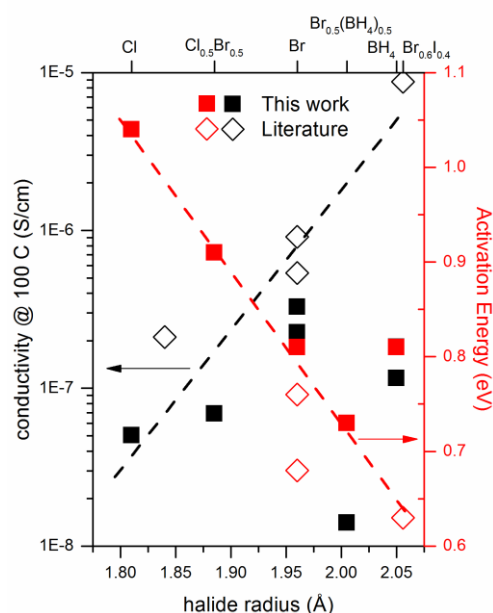


Figure 6: Plot of the log (σ) and activation energy versus A-site anion radii for several sodium-rich antiperovskites.

3.4. Structural and transport properties of Na₃OBH₄

Sun et al. [12] recently reported on Na₃OBH₄ synthesized by a similar procedure to the one used here and with a very high conductivity of the order of 10⁻³ S/cm at room temperature. This conductivity is ~10⁷ times higher than what we measured for multiple Na₃OBH₄ samples we synthesized (Figure 5), including one emulating exactly their synthesis parameters. In order to try and understand this inconsistency, we have performed additional characterization of the Na₃OBH₄ sample.

The existence of strong covalent B-H bonds in the BH₄⁻ subunit allows for the investigation of this material through vibrational spectroscopy. Raman and FTIR spectra of the Na₃OBH₄ sample are shown in Figure 7, as compared to those of the NaBH₄ reagent. Combining the two techniques the four normal modes of the BH₄⁻ tetrahedron, ν_1 - ν_4 , are clearly observable, further attesting its integration in the structure. Peaks below 1000 cm⁻¹ in the Raman spectrum likely correspond to vibrations of the sodium lattice with respect to the anion sublattice, attesting to Na⁺ mobility in the material. A peak at 1452 cm⁻¹ in the FTIR spectrum of Na₃OBH₄ remains unassigned, but was also observed for a Na₂(BH₄)(NH₂) antiperovskite sample in the literature and is likely a “combination of a fundamental and a lattice mode”[35].

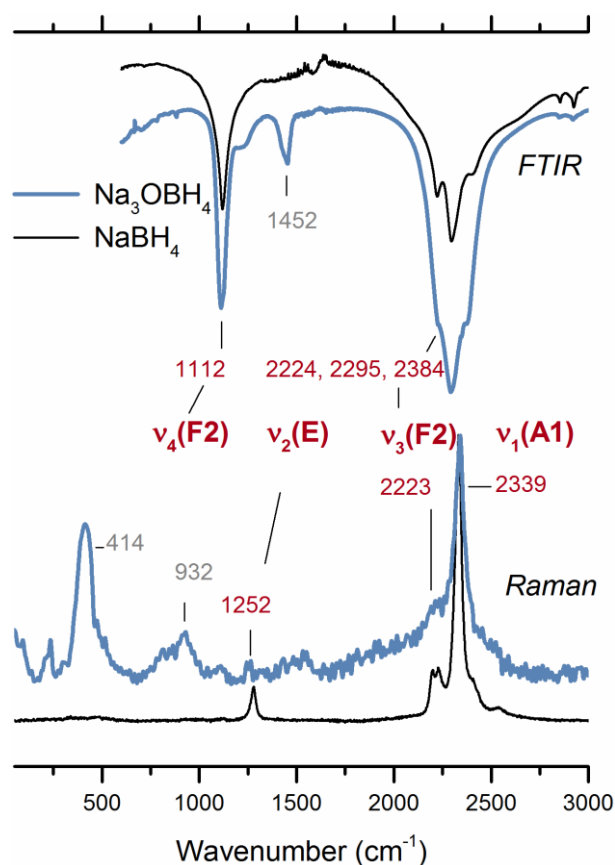


Figure 7: Vibrational (Raman and FTIR) spectra of annealed Na₃OBH₄ and NaBH₄ with assignments.

The thermograms of Na₃OBH₄ shown in Figure 8 do not reveal any sign of melting of the sample below 400 °C. This is in stark contrast with a melting temperature of 240 °C reported by Sun et al. [12]. Indeed, pelletized samples annealed at 300 °C maintained their shape and phase purity. Instead our thermograms show a sharp exothermic peak at 425 °C followed by a broad endothermic effect centered at 441 °C and a distinct rise of the baseline (i.e. heat capacity). The DSC peaks are coupled with a mass loss reaching ~4% by the end of the experiment. From the associated mass spectra (Fig.

S3), we identified the majority of the outgassing to be H_2 ($m/z=2$) along with traces of $m/z=13$, 14, 15 and 16 which are likely attributed to diborane B_2H_6 ($m/z=16$) and its molecular fragments. The above leads to an interpretation of the decomposition of Na_3OBH_4 at $425^\circ C$ rather than melting. It is noted that the total H content in Na_3OBH_4 corresponds to approximately 8% of its mass, i.e. ~50% of the hydrogen in the material was released during its thermal decomposition. Overall, the thermal analysis of our sample shows significantly different behavior than the one reported by Sun et al. [12].

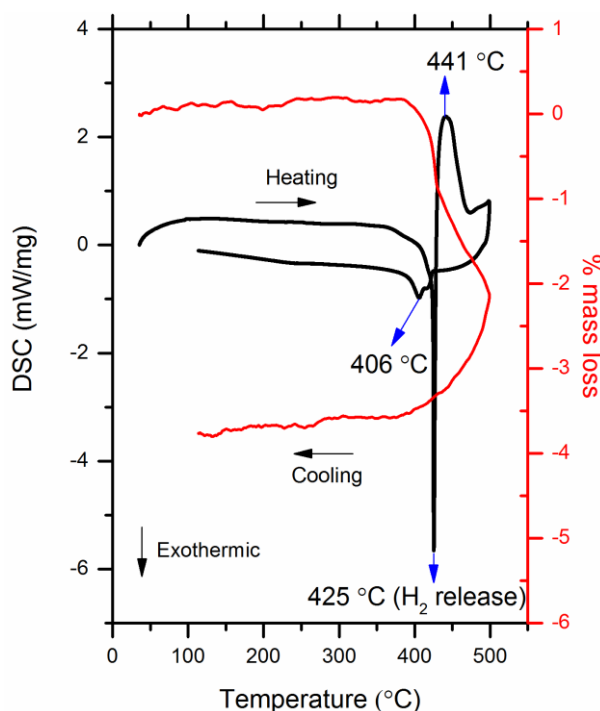


Figure 8: DSC and TGA of as-milled Na_3OBH_4

Despite the differences in thermal behavior, our diffractograms and vibrational spectra (Figs. 2 and 7) clearly indicate the purity of our product and agree in principle with the structural analysis of Sun et al. It is unclear at this point why we cannot replicate the electrical conductivity performance (and thermal behavior) previously reported. Sun et al. highlighted the importance of hot-pressing their pellets to reach the high conductivity reported. While it is plausible that hot pressing could alleviate the effects of blocking grain boundaries [23,24], it would be surprising for this difference in processing to account for 7 orders of magnitude difference in measured ionic conductivity between our work and theirs. We note that the lower conductivity we measure is closer in line with the conductivities of other sodium-rich antiperovskites reported here and elsewhere and seems to follow the qualitative trends with halide size and polarizability (Figs. 5 and 6).

The results from our AIMD simulations also present some significant differences to those of Sun et al. In the AIMD simulations of Sun et al., zero and two Na hops were reported at high temperatures of 700 and 900 K, respectively, for Na_3OBr , while for Na_3OBH_4 , two and five hops occurred at 700 and 900 K, respectively. These results suggest that the rate of Na-ion diffusion at >700 K is greater in Na_3OBH_4 compared to Na_3OBr , which is in contrast to our AIMD results presented in Figure 5b that suggest higher Na-ion diffusion in Na_3OBr above room temperature. This discrepancy may result from the fact that the AIMD simulations of Sun et al. were only carried out for 40 ps and with a small $2 \times 2 \times 2$ supercell. In contrast, the simulations we report here were performed for over 100 ps and a $3 \times 3 \times 3$ unit cell, greatly increasing the statistical significance of our conclusions.

Sun et al. attributed the excellent high conductivity they reported to a rotational motion (orientational freedom) of the BH_4^- anion [12]. This is in principle possible; such arguments of couple anionic/cationic mobility (paddle-wheel effect, crystal plasticity) have recently resurfaced in the context of borohydride [49–54] and sulfide [55–60] ion conductors for batteries. Our molecular dynamics simulations indeed show that the BH_4^- anion rotates at all the temperatures tested. Nevertheless the computed Na^+ diffusivities for Na_3OBH_4 are still of the same order of magnitude as those observed for other sodium-rich antiperovskites examined (Figure 5b), and are also in qualitative agreement with our impedance results (Figure 5a). Based on our analysis, we conclude that BH_4^- rotations are likely and could lead to a decreased activation energy for conduction. However, we cannot replicate the overall ionic conductivity or diffusivity of Na^+ previously reported, neither by experimental impedance measurements nor by AIMD simulations.

4. Conclusion

We have reported here the efficacy and efficiency of mechanochemistry (ball-milling) for the synthesis of a wide variety of sodium-rich antiperovskite materials, Na_3OX ($\text{X} = \text{Cl}, \text{Br}, \text{I}, \text{BH}_4$). Through utilization of pure Na_2O , these materials can be obtained in a single-step, without the need for annealing. Using our diffraction data, impedance spectroscopy and molecular dynamics simulations, we investigate the effect of halide substitution on the interrelated structural and ion transport properties of Na_3OX ($\text{X} = \text{Cl}, \text{Br}, \text{BH}_4$). We show that the (super)halogen size controls the lattice volume and implicitly the Na-ion conductivity of these materials. In parallel, the polarizability of the (super)halogen controls the activation energy for conduction through its effect on the lattice softness. We also examine the recent reports of high ionic conductivity in Na_3OBH_4 which we were unable to reproduce. Both our impedance spectroscopy experiments and molecular dynamics simulations indicate that Na_3OBH_4 is not a positive outlier in terms of its ion transport, and exhibits a similar Na-ion conductivity to other sodium-rich antiperovskites.

The ionic conductivities of the undoped materials measured in this fundamental study are of course still too low to envisage any practical application. Future perspectives to increase the ionic conductivity would include the utilization of larger, more polarizable anions on the six-coordinated site, e.g. replace the O^{2-} by S^{2-} . Although full sulfide compositions could not be synthesized, we show here that partial replacement of O^{2-} by S^{2-} is possible and leads to the expected increase in lattice volume. Future studies should investigate whether such substitution significantly affects ion transport. In addition, introducing vacancies by aliovalent substitutions of divalent cations (e.g. Mg^{2+} or Ca^{2+} [22,27]) on the sodium site has been proven to be an effective strategy to increase ionic conductivity. These strategies could be combined with the halide mixing demonstrated in this work to increase the ionic conductivity in sodium-rich antiperovskites.

5. Acknowledgements

E.H. acknowledges the RS2E (<https://www.energie-rs2e.com/en>) and CNRS for their financial support in the form of a 6-month internship scholarship in Amiens. T.F. acknowledges the Alistore ERI (<http://www.alistore.eu/>) and CNRS for their financial support in the form of a joint PhD scholarship between Amiens (France) and Bath (UK). J.A.D. and M.S.I. gratefully acknowledge the MCC/Archer consortium (EP/L000202/1) for computational resources. J.A.D. also gratefully acknowledges Newcastle University for funding through a Newcastle Academic Track (NUAct) Fellowship.

6. References

- [1] T. Famprikis, P. Canepa, J.A. Dawson, M.S. Islam, C. Masquelier, Fundamentals of inorganic solid-state electrolytes for batteries, *Nat. Mater.* 18 (2019) 1278–1291. doi:10.1038/s41563-019-0431-3.
- [2] Z. Zhang, Y. Shao, B. Lotsch, Y.-S. Hu, H. Li, J. Janek, L.F. Nazar, C. Nan, J. Maier, M. Armand, L. Chen, New horizons for inorganic solid state ion conductors, *Energy Environ. Sci.* 11 (2018) 1945–1976. doi:10.1039/C8EE01053F.
- [3] C. Zhao, L. Liu, X. Qi, Y. Lu, F. Wu, J. Zhao, Y. Yu, Y. Hu, L. Chen, Solid-State Sodium Batteries, *Adv. Energy Mater.* 8 (2018) 1703012. doi:10.1002/aenm.201703012.
- [4] S. Ohno, A. Banik, G.F. Dewald, M.A. Kraft, T. Krauskopf, N. Minafra, P. Till, M. Weiss, W.G. Zeier, Materials design of ionic conductors for solid state batteries, *Prog. Energy.* 2 (2020) 022001. doi:10.1088/2516-1083/ab73dd.
- [5] J.C. Bachman, S. Muy, A. Grimaud, H.H. Chang, N. Pour, S.F. Lux, O. Paschos, F. Maglia, S. Lupart, P. Lamp, L. Giordano, Y. Shao-Horn, Inorganic Solid-State Electrolytes for Lithium Batteries: Mechanisms and Properties Governing Ion Conduction, *Chem. Rev.* 116 (2016) 140–162. doi:10.1021/acs.chemrev.5b00563.
- [6] Y. Sun, P. Guan, Y. Liu, H. Xu, S. Li, D. Chu, Recent Progress in Lithium Lanthanum Titanate Electrolyte towards All Solid-State Lithium Ion Secondary Battery, *Crit. Rev. Solid State Mater. Sci.* 44 (2019) 265–282. doi:10.1080/10408436.2018.1485551.
- [7] Z. Wu, Z. Xie, A. Yoshida, Z. Wang, X. Hao, A. Abudula, G. Guan, Utmost limits of various solid electrolytes in all-solid-state lithium batteries: A critical review, *Renew. Sustain. Energy Rev.* 109 (2019) 367–385. doi:10.1016/j.rser.2019.04.035.
- [8] M.H. Braga, N.S. Grundish, A.J. Murchison, J.B. Goodenough, Alternative Strategy for a Safe Rechargeable Battery, *Energy Environ. Sci.* 10 (2016) 0–6. doi:10.1039/C6EE02888H.
- [9] Y. Li, W. Zhou, S. Xin, S. Li, J. Zhu, X. Lü, Z. Cui, Q. Jia, J. Zhou, Y. Zhao, J.B. Goodenough, Fluorine-Doped Antiperovskite Electrolyte for All-Solid-State Lithium-Ion Batteries, *Angew. Chemie Int. Ed.* 55 (2016) 9965–9968. doi:10.1002/anie.201604554.
- [10] M.H. Braga, A.J. Murchison, J.A. Ferreira, P. Singh, J.B. Goodenough, Glass-amorphous alkali-ion solid electrolytes and their performance in symmetrical cells, *Energy Environ. Sci.* 9 (2016) 948–954. doi:10.1039/C5EE02924D.
- [11] Y. Zhao, L.L. Daemen, Superionic Conductivity in Lithium-Rich Anti-Perovskites, *J. Am. Chem. Soc.* 134 (2012) 15042–15047. doi:10.1021/ja305709z.
- [12] Y. Sun, Y. Wang, X. Liang, Y. Xia, L. Peng, H. Jia, H. Li, L. Bai, J. Feng, H. Jiang, J. Xie, Rotational Cluster Anion Enabling Superionic Conductivity in Sodium-Rich Antiperovskite Na₃OBH₄, *J. Am. Chem. Soc.* 141 (2019) 5640–5644. doi:10.1021/jacs.9b01746.
- [13] A.S. Bhalla, R. Guo, R. Roy, The perovskite structure—a review of its role in ceramic science and technology, *Mater. Res. Innov.* 4 (2000) 3–26. doi:10.1007/s100190000062.
- [14] T.K. Schwietert, V.A. Arszewska, C. Wang, C. Yu, A. Vasileiadis, N.J.J. de Klerk, J. Hageman, T. Hupfer, I. Kerkamm, Y. Xu, E. van der Maas, E.M. Kelder, S. Ganapathy, M. Wagemaker, Clarifying the relationship between redox activity and electrochemical stability in solid electrolytes, *Nat. Mater.* (2020). doi:10.1038/s41563-019-0576-0.
- [15] Z. Deng, Z. Wang, I.-H. Chu, J. Luo, S.P. Ong, Elastic Properties of Alkali Superionic Conductor

- Electrolytes from First Principles Calculations, *J. Electrochem. Soc.* 163 (2016) A67–A74. doi:10.1149/2.0061602jes.
- [16] E. Zintl, W. Morawietz, Orthosalze von Sauerstoffsäuren, *Zeitschrift Für Anorg. Und Allg. Chemie.* 236 (1938) 372–410. doi:10.1002/zaac.19382360134.
- [17] A. Klemenc, V. Gutmann, Zur Kenntnis der Salpetersäure IX. Über Orthonitrit und Orthonitrat, *Monatshefte Für Chemie.* 81 (1950) 361–371. doi:10.1007/BF00903039.
- [18] M. Jansen, Neue Untersuchungen an Na_3NO_3 , *Zeitschrift Für Anorg. Und Allg. Chemie.* 435 (1977) 13–20. doi:10.1002/zaac.19774350102.
- [19] H. Sabrowsky, K. Paszkowski, D. Reddig, P. Vogt, Na_3OCl und Na_3OBr , die ersten Alkalimetallchalkogenidhalogenide / Na_3OCl and Na_3OBr , the First Alkali Metal Chalcogenide Halides, *Zeitschrift Für Naturforsch. B.* 43 (1988) 238–239. doi:10.1515/znb-1988-0217.
- [20] W. Müller, M. Jansen, $(\text{CN})\text{ONa}_3$, Kristallstruktur und Natriumionenleitfähigkeit, *Zeitschrift Für Anorg. Und Allg. Chemie.* 591 (1990) 41–46. doi:10.1002/zaac.19905910105.
- [21] M. Jansen, C. Feldmann, W. Müller, Über die quasi-binären Systeme $\text{NaNO}_2/\text{Na}_2\text{O}$ und $\text{NaCN}/\text{Na}_2\text{O}$. Phasendiagramme und Natrium-Ionenleitung in $\text{Na}_3\text{O}(\text{NO}_2)$ und $\text{Na}_3\text{O}(\text{CN})$, *Zeitschrift Für Anorg. Und Allg. Chemie.* 611 (1992) 7–10. doi:10.1002/zaac.19926110502.
- [22] Y. Wang, Q. Wang, Z. Liu, Z. Zhou, S. Li, J. Zhu, R. Zou, Y. Wang, J. Lin, Y. Zhao, Structural manipulation approaches towards enhanced sodium ionic conductivity in Na-rich antiperovskites, *J. Power Sources.* 293 (2015) 735–740. doi:10.1016/j.jpowsour.2015.06.002.
- [23] H. Nguyen, S. Hy, E. Wu, Z. Deng, M. Samiee, T. Yersak, J. Luo, S.P. Ong, Y.S. Meng, Experimental and Computational Evaluation of a Sodium-Rich Anti-Perovskite for Solid State Electrolytes, *J. Electrochem. Soc.* 163 (2016) A2165–A2171. doi:10.1149/2.0091610jes.
- [24] J.A. Dawson, P. Canepa, T. Famprikis, C. Masquelier, M.S. Islam, Atomic-Scale Influence of Grain Boundaries on Li-Ion Conduction in Solid Electrolytes for All-Solid-State Batteries, *J. Am. Chem. Soc.* 140 (2018) 362–368. doi:10.1021/jacs.7b10593.
- [25] J.A. Dawson, T.S. Attari, H. Chen, S.P. Emge, K.E. Johnston, M.S. Islam, Elucidating lithium-ion and proton dynamics in anti-perovskite solid electrolytes, *Energy Environ. Sci.* 11 (2018) 2993–3002. doi:10.1039/C8EE00779A.
- [26] A. Emly, E. Kioupakis, A. Van der Ven, Phase Stability and Transport Mechanisms in Antiperovskite Li_3OCl and Li_3OBr Superionic Conductors, *Chem. Mater.* 25 (2013) 4663–4670. doi:10.1021/cm4016222.
- [27] T.H. Wan, Z. Lu, F. Ciucci, A first principle study of the phase stability, ion transport and substitution strategy for highly ionic conductive sodium antiperovskite as solid electrolyte for sodium ion batteries, *J. Power Sources.* 390 (2018) 61–70. doi:10.1016/j.jpowsour.2018.03.073.
- [28] J.A. Dawson, H. Chen, M. Saiful Islam, Composition Screening of Lithium- and Sodium-Rich Anti-Perovskites for Fast-Conducting Solid Electrolytes, *J. Phys. Chem. C.* 122 (2018) 23978–23984. doi:10.1021/acs.jpcc.8b08208.
- [29] J. Zhu, Y. Wang, S. Li, J.W. Howard, J. Neuefeind, Y. Ren, H. Wang, C. Liang, W. Yang, R. Zou, C. Jin, Y. Zhao, Sodium Ion Transport Mechanisms in Antiperovskite Electrolytes Na_3OBr and Na_4OI_2 : An in Situ Neutron Diffraction Study, *Inorg. Chem.* 55 (2016) 5993–5998. doi:10.1021/acs.inorgchem.6b00444.
- [30] T.-L. Pham, A. Samad, H.J. Kim, Y.-H. Shin, Computational predictions of stable phase for

- antiperovskite Na_3OCl via tilting of Na_6O octahedra, *J. Appl. Phys.* 124 (2018) 164106. doi:10.1063/1.5047833.
- [31] D. Siegel, K. Kim, Correlating Lattice Distortions, Ion Migration Barriers, and Stability in Solid Electrolytes, *J. Mater. Chem. A.* (2019). doi:10.1039/C8TA10989C.
- [32] Y. Yu, Z. Wang, G. Shao, Theoretical design of double anti-perovskite Na_6SOI_2 as a super-fast ion conductor for solid Na^+ ion batteries, *J. Mater. Chem. A.* 6 (2018) 19843–19852. doi:10.1039/C8TA08412B.
- [33] H. Fang, P. Jena, Sodium Superionic Conductors Based on Clusters, *ACS Appl. Mater. Interfaces.* 11 (2019) 963–972. doi:10.1021/acsami.8b19003.
- [34] M.S. Avdontceva, A. a. Zolotarev, S. V. Krivovichev, Order–disorder phase transition in the antiperovskite-type structure of synthetic kogarkoite, $\text{Na}_3\text{SO}_4\text{F}$, *J. Solid State Chem.* 231 (2015) 42–46. doi:10.1016/j.jssc.2015.07.033.
- [35] M. Somer, S. Acar, C. Koz, I. Kokal, P. Höhn, R. Cardoso-Gil, U. Aydemir, L. Akselrud, α - and β - $\text{Na}_2[\text{BH}_4][\text{NH}_2]$: Two modifications of a complex hydride in the system NaNH_2 – NaBH_4 ; syntheses, crystal structures, thermal analyses, mass and vibrational spectra, *J. Alloys Compd.* 491 (2010) 98–105. doi:10.1016/j.jallcom.2009.10.268.
- [36] T. Famprikis, J. Galipaud, O. Clemens, B. Pecquenard, F. Le Cras, Composition Dependence of Ionic Conductivity in $\text{LiSiPO}(\text{N})$ Thin-Film Electrolytes for Solid-State Batteries, *ACS Appl. Energy Mater.* 2 (2019) 4782–4791. doi:10.1021/acsaem.9b00415.
- [37] G. Kresse, J. Furthmüller, Efficient iterative schemes for ab initio total-energy calculations using a plane-wave basis set, *Phys. Rev. B.* 54 (1996) 11169–11186. doi:10.1103/PhysRevB.54.11169.
- [38] P.E. Blöchl, Projector augmented-wave method, *Phys. Rev. B.* 50 (1994) 17953–17979. doi:10.1103/PhysRevB.50.17953.
- [39] J.P. Perdew, A. Ruzsinszky, G.I. Csonka, O.A. Vydrov, G.E. Scuseria, L.A. Constantin, X. Zhou, K. Burke, Restoring the Density-Gradient Expansion for Exchange in Solids and Surfaces, *Phys. Rev. Lett.* 100 (2008) 136406. doi:10.1103/PhysRevLett.100.136406.
- [40] D.J. Evans, B.L. Holian, The Nose–Hoover thermostat, *J. Chem. Phys.* 83 (1985) 4069–4074. doi:10.1063/1.449071.
- [41] V.M. Goldschmidt, Die Gesetze der Krystallochemie, *Naturwissenschaften.* 14 (1926) 477–485. doi:10.1007/BF01507527.
- [42] K. Hippler, S. Sitta, P. Vogt, H. Sabrowsky, Structure of Na_3OCl , *Acta Crystallogr. Sect. C Cryst. Struct. Commun.* 46 (1990) 736–738. doi:10.1107/S010827018900990X.
- [43] R.D. Shannon, Revised effective ionic radii and systematic studies of interatomic distances in halides and chalcogenides, *Acta Crystallogr. Sect. A.* 32 (1976) 751–767. doi:10.1107/S0567739476001551.
- [44] H.K. Roobottom, H.D.B. Jenkins, J. Passmore, L. Glasser, Thermochemical Radii of Complex Ions, *J. Chem. Educ.* 76 (1999) 1570. doi:10.1021/ed076p1570.
- [45] Ö.U. Kudu, T. Famprikis, B. Fleutot, M.-D. Braidă, T. Le Mercier, M.S. Islam, C. Masquelier, A review of structural properties and synthesis methods of solid electrolyte materials in the Li_2S – P_2S_5 binary system, *J. Power Sources.* 407 (2018) 31–43. doi:10.1016/j.jpowsour.2018.10.037.

- [46] S. Ohno, T. Bernges, J. Buchheim, M. Duchardt, A.-K. Hatz, M.A. Kraft, H. Kwak, A.L. Santhosha, Z. Liu, N. Minafra, F. Tsuji, A. Sakuda, R. Schlem, S. Xiong, Z. Zhang, P. Adelhelm, H. Chen, A. Hayashi, Y.S. Jung, B. V. Lotsch, B. Roling, N.M. Vargas-Barbosa, W.G. Zeier, How Certain Are the Reported Ionic Conductivities of Thiophosphate-Based Solid Electrolytes? An Interlaboratory Study, *ACS Energy Lett.* 5 (2020) 910–915. doi:10.1021/acsenergylett.9b02764.
- [47] R. Kanno, M. Murayama, Lithium Ionic Conductor Thio-LISICON: The $\text{Li}_2\text{S-GeS}_2\text{-P}_2\text{S}_5$ System, *J. Electrochem. Soc.* 148 (2001) A742. doi:10.1149/1.1379028.
- [48] M.A. Kraft, S.P. Culver, M. Calderon, F. Böcher, T. Krauskopf, A. Senyshyn, C. Dietrich, A. Zevalkink, J. Janek, W.G. Zeier, Influence of Lattice Polarizability on the Ionic Conductivity in the Lithium Superionic Argyrodites $\text{Li}_6\text{PS}_5\text{X}$ (X = Cl, Br, I), *J. Am. Chem. Soc.* 139 (2017) 10909–10918. doi:10.1021/jacs.7b06327.
- [49] Y. Sadikin, P. Schouwink, M. Brighi, Z. Łodziana, R. Černý, Modified Anion Packing of $\text{Na}_2\text{B}_{12}\text{H}_{12}$ in Close to Room Temperature Superionic Conductors, *Inorg. Chem.* 56 (2017) 5006–5016. doi:10.1021/acs.inorgchem.7b00013.
- [50] A.V. Soloninin, R.V. Skoryunov, O.A. Babanova, A.V. Skripov, M. Dimitrievska, T.J. Udovic, Comparison of anion and cation dynamics in a carbon-substituted closo-hydroborate salt: ^1H and ^{23}Na NMR studies of solid-solution $\text{Na}_2(\text{CB}_9\text{H}_{10})(\text{CB}_{11}\text{H}_{12})$, *J. Alloys Compd.* 800 (2019) 247–253. doi:10.1016/j.jallcom.2019.06.019.
- [51] L. Duchêne, S. Lunghammer, T. Burankova, W.-C. Liao, J.P. Embs, C. Copéret, H.M.R. Wilkening, A. Remhof, H. Hagemann, C. Battaglia, Ionic Conduction Mechanism in the $\text{Na}_2(\text{B}_{12}\text{H}_{12})_{0.5}(\text{B}_{10}\text{H}_{10})_{0.5}$ closo -Borate Solid-State Electrolyte: Interplay of Disorder and Ion–Ion Interactions, *Chem. Mater.* 31 (2019) 3449–3460. doi:10.1021/acs.chemmater.9b00610.
- [52] M. Dimitrievska, P. Shea, K.E. Kweon, M. Bercx, J.B. Varley, W.S. Tang, A. V. Skripov, V. Stavila, T.J. Udovic, B.C. Wood, Carbon Incorporation and Anion Dynamics as Synergistic Drivers for Ultrafast Diffusion in Superionic $\text{LiCB}_{11}\text{H}_{12}$ and $\text{NaCB}_{11}\text{H}_{12}$, *Adv. Energy Mater.* 8 (2018) 1703422. doi:10.1002/aenm.201703422.
- [53] M. Brighi, F. Murgia, Z. Łodziana, P. Schouwink, A. Wołczyk, R. Cerny, A mixed anion hydroborate/carba-hydroborate as a room temperature Na-ion solid electrolyte, *J. Power Sources.* 404 (2018) 7–12. doi:10.1016/j.jpowsour.2018.09.085.
- [54] Y. Yan, R.-S. Kühnel, A. Remhof, L. Duchêne, E.C. Reyes, D. Rentsch, Z. Łodziana, C. Battaglia, A Lithium Amide-Borohydride Solid-State Electrolyte with Lithium-Ion Conductivities Comparable to Liquid Electrolytes, *Adv. Energy Mater.* 1700294 (2017) 1700294. doi:10.1002/aenm.201700294.
- [55] J.G. Smith, D.J. Siegel, Low-temperature paddlewheel effect in glassy solid electrolytes, *Nat. Commun.* 11 (2020) 1483. doi:10.1038/s41467-020-15245-5.
- [56] I. Hanghofer, B. Gadermaier, H.M.R. Wilkening, Fast Rotational Dynamics in Argyrodite-Type $\text{Li}_6\text{PS}_5\text{X}$ (X: Cl, Br, I) as Seen by ^{31}P Nuclear Magnetic Relaxation—On Cation–Anion Coupled Transport in Thiophosphates, *Chem. Mater.* 31 (2019) 4591–4597. doi:10.1021/acs.chemmater.9b01435.
- [57] Z. Zhang, P. Roy, H. Li, M. Avdeev, L.F. Nazar, Coupled Cation–Anion Dynamics Enhances Cation Mobility in Room-Temperature Superionic Solid-State Electrolytes, *J. Am. Chem. Soc.* 141 (2019) 19360–19372. doi:10.1021/jacs.9b09343.
- [58] G.K. Phani Dathar, J. Balachandran, P.R.C. Kent, A.J. Rondinone, P. Ganesh, Li-ion site disorder

driven superionic conductivity in solid electrolytes: a first-principles investigation of β -Li₃PS₄,
J. Mater. Chem. A. 5 (2017) 1153–1159. doi:10.1039/C6TA07713G.

- [59] S. Adams, R. Prasada Rao, Structural requirements for fast lithium ion migration in Li₁₀GeP₂S₁₂,
J. Mater. Chem. 22 (2012) 7687. doi:10.1039/c2jm16688g.
- [60] T. Famprikis, J.A. Dawson, F. Fauth, O. Clemens, E. Suard, B. Fleutot, M. Courty, J.-N. Chotard,
M.S. Islam, C. Masquelier, A New Superionic Plastic Polymorph of the Na⁺ Conductor Na₃PS₄,
ACS Mater. Lett. 1 (2019) 641–646. doi:10.1021/acsmaterialslett.9b00322.